

A Generalized Framework for Critical Heat Flux Detection Using Unsupervised Image-to-Image Translation

Firas Al-Hindawi^a (falhinda@asu.edu), Tejaswi Soori^b (ts3396@drexel.edu),
Han Hu^c (hanhu@uark.edu), Md Mahfuzur Rahman Siddiquee^a
(mrahmans@asu.edu), Hyunsoo Yoon^d (hs.yoon@yonsei.ac.kr), Teresa Wu^a
(teresa.wu@asu.edu), Ying Sun^b (ys347@drexel.edu)

^a Arizona State University, 699 Mill Avenue, Tempe, AZ 85281, US

^b Drexel University, 3141 Chestnut Street, Philadelphia, PA 19104, US

^c University of Arkansas, 1 University of Arkansa, Fayetteville, AR 72701, US

^d Yonsei University, D301 50 Yonsei-ro, Seodaemun-gu, Seoul, 03722, South Korea

Corresponding Author:

Firas Al-Hindawi

Arizona State University, 699 Mill Avenue, Tempe, AZ 85281, US

Tel: +1 (602) 837-9820

Email: falhinda@asu.edu

A Generalized Framework for Critical Heat Flux Detection Using Unsupervised Image-to-Image Translation

Firas Al-Hindawi^{a,*}, Tejaswi Soori^b, Han Hu^c, Md Mahfuzur Rahman Siddiquee^a, Hyunsoo Yoon^d, Teresa Wu^a, Ying Sun^b

^aArizona State University, 699 Mill Avenue, Tempe, AZ 85281, US

^bDrexel University, 3141 Chestnut Street, Philadelphia, PA 19104, US

^cUniversity of Arkansas, 1 University of Arkansas, Fayetteville, AR 72701, US

^dYonsei University, D301 50 Yonsei-ro, Seodaemun-gu, Seoul, 03722, South Korea

Abstract

This work proposes a framework developed to generalize Critical Heat Flux (CHF) detection classification models using an Unsupervised Image-to-Image (UI2I) translation model. The framework enables a typical classification model that was trained and tested on boiling images from domain A to predict boiling images coming from domain B that was never seen by the classification model. This is done by using the UI2I model to transform the domain B images to look like domain A images that the classification model is familiar with. Although CNN was used as the classification model and Fixed-Point GAN (FP-GAN) was used as the UI2I model, the framework is model agnostic. Meaning, that the framework can generalize any image classification model type, making it applicable to a variety of similar applications and not limited to the boiling crisis detection problem. It also means that the more the UI2I models advance, the better the performance of the framework.

Keywords: Critical Heat Flux, Domain Adaptation, Generative Adversarial Networks, Image-to-Image Translation, Pool Boiling, Unsupervised Machine

*Corresponding author.

Email addresses: falhinda@asu.edu (Firas Al-Hindawi), ts3396@drexel.edu (Tejaswi Soori), hanhu@uark.edu (Han Hu), mrahmans@asu.edu (Md Mahfuzur Rahman Siddiquee), hs.yoon@yonsei.ac.kr (Hyunsoo Yoon), teresa.wu@asu.edu (Teresa Wu), ys347@drexel.edu (Ying Sun)

1. Introduction

Boiling is a heat transfer mechanism that dissipates a large amount of heat with minimal temperature increase by taking the advantage of the latent heat of the working fluid. As such, boiling has been widely implemented. Nevertheless, the heat flux of boiling is bounded by a practical limit known as the critical heat flux (CHF), beyond which, a continuous vapor layer will blanket the heater surface, leading to a significant reduction in heat transfer coefficient (HTC) and deteriorating the heat dissipation; this process is also known as the critical heat flux (a.k.a. boiling crisis). Upon the occurrence of CHF, a rapid temperature ramp takes place on the heater surface which will lead to detrimental device failures. To capture CHF, a variety of theoretical models have been developed based on different transport mechanisms during boiling, including hydrodynamic instabilities (Zuber, 1959), force balance (Kandlikar, 2001), etc. However, due to the complexity and stochasticity of the boiling process, existing theoretical CHF models are overly-simplified to accurately predict CHF before it happens. Often, a safety factor (e.g. the departure from the nucleate boiling ratio (DNBR) in nuclear reactors) is applied to avoid the boiling crisis, leading to reduced system performance (Lee et al., 2021).

Boiling images have attracted great attention lately as the images contain detailed information on the bubble dynamics. It is of both fundamental and practical interest to detect the CHF and identify the dominant transport mechanism that triggers CHF using boiling images. In the side view boiling images, bubbles at different locations are at different stages of the ebullition cycle. As such, under steady-state conditions, the dynamics of the bubbles are embedded in static boiling images. A static image of pool boiling may cover the entire ebullition cycle, including bubble nucleation, growth, and departure. Traditional analysis of the boiling images relies on the extraction of physical parameters based on domain knowledge, such as bubble size, bubble departure frequency (Li et al.,

2019), nucleation site density (Park et al., 2016), void fraction (Ridwan & McCarthy, 2019), vapor film (Allred et al., 2018), etc. But the stochasticity of the bubble dynamics adds to the fluctuations and uncertainties of the extracted physical parameters. Furthermore, the traditional boiling image analysis is limited to known physical parameters, whereas it is not clear whether the known parameters are sufficient to capture the boiling crisis.

Recent advances in machine learning (ML) and deep learning (DL) algorithms have enabled researchers to apply these algorithms in a wide variety of engineering applications (Altarazi et al., 2019; Alhindawi & Altarazi, 2018; Rokoni et al., 2022; Rassoulinejad-Mousavi et al., 2021; Zhao et al., 2022; Ji et al., 2022; Wang et al., 2022). One of these applications is the real-time detection of boiling heat flux and CHF. ML/DL models have been developed to predict boiling heat flux or/and the boiling regime with acoustic emissions (Sinha et al., 2021), optical images (Rokoni et al., 2022), thermographs (Ravichandran et al., 2021) using a variety of supervised learning algorithms, including support vector machine (Hobold & Silva, 2018), multilayer perceptron (MLP) neural networks (Hobold & Silva, 2018), and convolutional neural networks (CNN) (Rassoulinejad-Mousavi et al., 2021). While existing studies have shown these models with high prediction accuracy, most of the models are only trained and tested on single-source dataset, e.g., the authors' own experimental data. It is known that supervised learning models yield high performance only when the target testing data come from the same distribution as the source training data. For applications where the target data are drawn from a different distribution than the source training data, the performance of the model declines dramatically and in extreme cases, it may become worse than random guessing (Wilson & Cook, 2020). We contend the generalizability and adaptability of the ML/DL models for boiling crisis detection remain a key challenge. Recently, transfer learning (TL) is used to adapt a trained CNN model for boiling regime classification to a new target domain with a small volume of labeled data from the target domain (Rassoulinejad-Mousavi et al., 2021). By taking features from the trained CNN model and fine-tuning the networks, the TL model requires

much less labeled data from the target domain than CNN to yield the same level of prediction accuracy. Nevertheless, this TL approach still relies on labeled data from the target domain and is not applicable to an unlabeled target domain.

To resolve this issue, unsupervised transfer learning is needed to adapt a trained model to unlabeled target domains. Researchers are motivated to explore the single-source homogenous unsupervised deep domain adaptation problem (Wilson & Cook, 2020). Most unsupervised deep domain adaptation methodologies prevail by either designing new distance metrics to measure the discrepancy between two domains to minimize the discrepancy between the domains or by learning domain invariant features using adversarial learning-based methods inspired by generative adversarial networks (GANs). Ever since Goodfellow et al.’s seminal work in 2014 (Goodfellow et al., 2014), GAN has been updated and leveraged in a wide range of applications. Recently, GANs have been gaining a lot of attraction and have been utilized in Unsupervised Image-to-Image (UI2I) translation. The development of CycleGAN (Zhu et al., 2017) made a breakthrough by introducing cycle consistency which made UI2I translation possible. However, it requires two dedicated generators for each pair of images making it difficult to scale in problems dealing with many domains. StarGAN (Choi et al., 2018) overcame this issue by introducing multi-domain image-to-image translation using a single generator and discriminator network. However, StarGAN tends to change the images unnecessarily during image-to-image translation even when no translation is required (Siddiquee et al., 2019). To address this issue, Siddiquee et al. (Siddiquee et al., 2019) proposed a new GAN variant termed Fixed-Point GAN (FP-GAN). This FP-GAN framework focused on identifying a minimal subset of pixels for domain translation and introduced fixed-point translation by supervising same-domain translation through a conditional identity loss, and regularizing cross-domain translation through revised adversarial, domain classification, and cycle consistency loss. Because of its convenience, the application of unsupervised domain adaptation in different fields has been very popular recently. Researchers have been utiliz-

ing it in various applications, such as fault diagnosis in gearboxes (Deng et al., 2019) and bearings (Deng et al., 2022; Xu et al., 2022) and in the Industrial Internet of Things (IIoT) networks security (Hassan et al., 2021-04).

Nevertheless, the utilization of GANs and unsupervised domain adaptation methods to study heat transfer processes has been rather limited and the specific use of UI2I translation models is even more scarce. albeit several novel applications of the method can be found in studying fluid dynamics problems such as unsteady flows, turbulence closure models, and flow field visualization. Li et al (Li et al., 2019) used an image-based, combined supervised-unsupervised DL algorithm to predict the heat transfer performance of a 3D plate-fin heat sink, where a CNN (the supervised part) was used to classify the temperature distribution images obtained from simulations based on the maximum temperature, and the GAN (the unsupervised part) was used to generate optimized ‘pseudo’ temperature distribution images. In the area of fluid dynamics, GANs were used to reconstruct high-fidelity data from low-fidelity Particle Image Velocimetry (PIV) data for flow around single and multiple cylinders (Deng et al., 2019), predicting unsteady flow around a cylinder where the GAN method can reproduce flow fields that match Large Eddy Simulations (LES) (Lee & You, 2019), as well as to study turbulent reactive flows using unsupervised DL trained with adversarial and physics-informed losses (Bode et al., 2021).

In this paper, we introduce a framework for generalizing classification models utilizing a UI2I translation model with CHF detection as the target task. While the classification model is CNN and the UI2I model is FP-GAN, we contend the framework is model agnostic. The framework is built on the assumption of having two datasets, a source dataset that is labeled and a target dataset that is not. The framework consists of two parts. The first part utilizes a typical classification model that is trained and tested on the source dataset. The second part utilizes an Unsupervised Image-to-Image (UI2I) translation model to transform images in the target dataset to look as if they were obtained from the same domain of the source dataset. This way, instead of investing in labeling every new dataset of interest and training a separate classification

model for each dataset, we could generalize the classification model at hand by adapting the new dataset to the domain that the classification model is familiar with, without the need for human supervision. A total of three datasets from different domains were used. Two of which were publicly available datasets (DS-1 and DS-2) and the third was obtained from in-house experiments (DS-3). We used the public dataset with the lowest resolution (DS-1) as our source dataset and alternated DS-2 and DS-3 with higher resolution images as the target dataset. This demonstrates the ability of the framework to work even from low resolution to high resolution and even when using publicly available datasets as the base.

To summarize, the contribution of this paper includes:

- Introducing an unsupervised domain adaptation framework to generalize a pre-trained classification model to unlabeled datasets coming from domains never seen previously by the classification model.
- The framework was applied to generalize a CNN classification model, but it is model agnostic and could be applied to any type of classification models.
- The framework used FP-GAN for UI2I translation, but it is agnostic to the UI2I model used. FP-GAN could be replaced by any other model. This means that the more the UI2I models advance, the better the performance of the framework.
- Although the framework was developed to solve the boiling crisis detection problem, it is a generalized framework applicable to other applications.

The paper is organized as follows, we first discuss the FP-GAN and the framework introduced in the Methods section. Next, we present the experiments section where we discuss data preparation, the source CNN model training, the FP-GAN model training, followed by the experiments conducted and their results. In Section 4, we discuss our findings and analysis of the results before we finally conclude the paper.

2. METHODS

The framework consists of two components: (1) The first component utilizes a typical classification model that is trained and tested on the source dataset; (2) The second component uses a UI2I translation model to transform images in the target dataset to look as if they were obtained from the same domain of the source dataset. In this paper, we will be using FP-GAN as our UI2I translation model and a CNN model as our classification model. This way, instead of generalizing the classification model by training it on hundreds of labeled datasets (which is infeasible) we can use this framework to make the data adapt to a pre-existing model. Although we are using this framework on boiling image datasets, the concept could be easily translated to any case scenario where there exists a pre-trained model on one domain that needs to be generalized to datasets from other domains. Fig1 summarizes the framework, where the classification training section is in red and the FP-GAN UI2I translation model training is in blue. The yellow-colored section is for testing.

Fig2 illustrates the Fixed-Point GAN architecture (FP-GAN). It contains a generator (denoted as G) and a discriminator network (denoted as D). The generator network G takes in an image with a target domain and translates it into an image in the source domain. The discriminator network D takes the generated image as input and evaluates if it looks real. The generator network G uses the feedback from the discriminator network D and improves the quality of the generated images. In the training setup, we improve the discriminator network for five iterations and then the generator network for one iteration using feedback from the discriminator network. We keep iterating these steps until the generated images look real.

The discriminator network D takes an image as input and produces two outputs: 1) whether the input image is real or fake and 2) the domain of the input image. For the first output, we train the discriminator network D by inputting the real images and recognizing them as real, as well as, the generated images to recognize them as fake. It is achieved by using the following loss

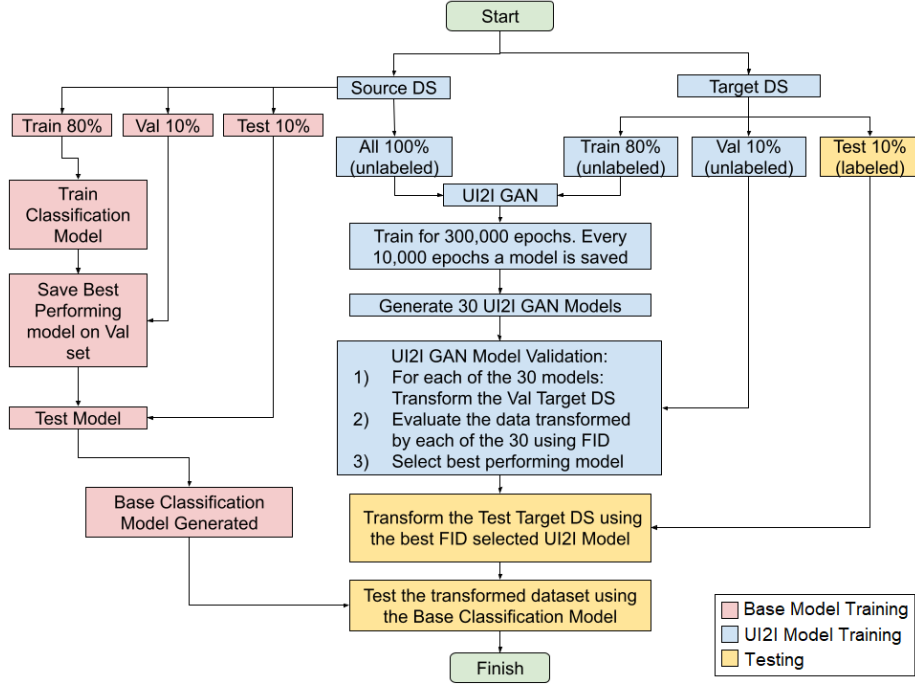


Figure 1: Framework Summary Flow Chart.

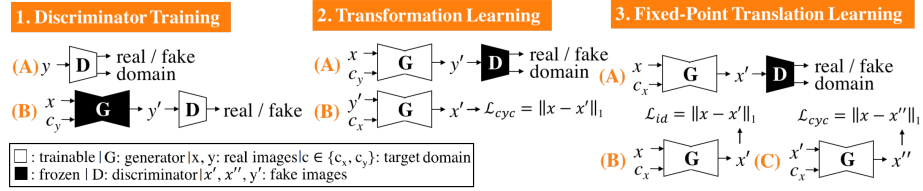


Figure 2: Visualization of Fixed-Point GAN training scheme (Siddiquee et al., 2019)

function:

$$L_{adv}^D = E_{x,c} [D_{\text{real/fake}} (G(x, c))] - E_x [D_{\text{real/fake}} (x)]$$

Here, x is an input image, c is a target domain from the set of all domains available in the dataset. We denote the real/fake output from the discriminator network as $D_{\text{real/fake}}$.

The discriminator network D , for the second output, is trained only using

the real images as input and their domain. The discriminator is supervised using the following loss function:

$$L_{\text{domain}}^D = E_{x,c_x} [-\log D_{\text{domain}}(c_x | x)]$$

Here, D_{domain} denotes the discriminator’s output for domain classification and c_x denotes the domain of the input image x .

The generator network G aims to translate the input image to the target domain in such a way that the minimal amount of modification in the input image is performed. Hence, the generator network G is trained for two types of transformations: 1) cross-domain translation and 2) same-domain translation. The cross-domain translation aims to train the generator network G to translate the input image to a different domain. The same-domain translation, on the other hand, regularize the cross-domain by training the generator to perform identity transformation of the input image. Since the generator network is trained without any input-output image pairs, the Fixed-Point GAN employs several regularizations during the generator training:

1. Adversarial Loss: This loss function takes the discriminator network’s feedback to improve the quality of the generated images. In other words, the generator network learns to match the generated images’ distribution to the real images’ distribution. Adversarial loss is defined as follows:

$$L_{adv}^G = - \sum_{c \in \{c_x, c_y\}} E_{x,c} [D_{\text{real} / \text{fake}}(G(x, c))]$$

2. Domain Classification Loss: In addition to generating real images, Fixed-Point GAN also needs to make sure that the generated images are in the correct domain as well. For this purpose, we again use the discriminator network’s feedback but only from the domain classification branch. Thus the constraints are defined as follows:

$$L_{\text{domain}}^G = \sum_{c \in \{c_x, c_y\}} E_{x,c} [-\log D_{\text{domain}}(c | G(x, c))]$$

3. Cycle-consistency Loss: Since our dataset is unpaired, optimizing the generator only with adversarial loss does not guarantee to preserve the content of the original image. Therefore, there are multiple but random solutions. Cycle consistency constraints make sure that the generator finds a unique solution and generates a such image that can be translated back to the original input image. The cycle-consistency loss is defined as:

$$L_{cyc} = E_{x,c_x,c_y} [||G(G(x, c_y), c_x) - x||_1] + E_{x,c_x} [||G(G(x, c_x), c_x) - x||_1]$$

4. Conditional Identity Loss: The identity loss can only be applied during the same-domain translation as the input and the output are expected to be the same. That’s why it is called conditional. It is defined as the following:

$$L_{id} = \begin{cases} 0, & c = c_y \\ E_{x,c} [||G(x, c) - x||_1], & c = c_x \end{cases}$$

Combining all the constraints described above, the complete objective function for both discriminator and generator networks can be described below:

$$L_D = L_{adv}^D + \lambda_{domain} L_{domain}^D$$

$$L_G = L_{adv}^G + \lambda_{domain} L_{domain}^G + \lambda_{cyc} L_{cyc} + \lambda_{id} L_{id}$$

Here, the λ s are the relative importance of each of the constraints to the full objective and they are hyperparameters thus selected empirically.

3. Experiments

3.1. Data Preparation

Three different pool boiling experimental image datasets (DS-1, DS-2, and DS-3) were prepared in this study, where DS-1 and DS-2 were generated using publicly available YouTube videos (You, 2014; Minseok et al., 2014) while DS-3 was conducted in-house. Specifically, the video from which DS-1 was prepared shows a pool boiling experiment performed using a square heater made of

high-temperature, thermally-conductive microporous coated copper where the surface was fabricated by sintering copper powder. The square heater had a surface area of $\approx 100 \text{ mm}^2$ and the working fluid used was water. All experiments were performed at a steady-state under an ambient pressure of 1 atm. A T-type thermocouple was used for temperature measurements. The resolution of the video frames was 512 x 480 pixels. The YouTube video from which DS-2 was prepared shows a pool boiling experiment performed using a circular heater made of microporous coated copper where the surface was fabricated by sintering copper powder. The circular heater had a diameter of $\approx 16 \text{ mm}$ and the working fluid used was DI water. All experiments were performed at a steady state under an ambient pressure of 0.5 atm. A T-type thermocouple was used for temperature measurements. The resolution of the video frames was 1280 x 20 pixels. DS-3 was obtained from our in-house experiments of water boiling on polished copper surfaces with an area of 100 mm^2 . The high-speed videos were captured using Phantom VEO 710L at a frame rate of 3000 fps and a resolution of 1280×800 pixels.

Images for DS-1 and DS-2 were prepared by downloading the videos from YouTube and extracting individual frames using a MATLAB code via the VideoReader and imwrite functions. Recognizing duplicate frames extracted from the YouTube videos, quality control was conducted to remove the repeated images by calculating the relative difference using the Structural Similarity Index (SSIM) value (Gao et al., 2020) between two consecutive images where images with a relative difference less than 0.03% were removed. This pre-processing is important to ensure DL models were not biased by identical image frames. Benefiting from the large optical sensor size ($25.6 \text{ mm} \times 16 \text{ mm}$) and the high-power backlight (Advanced Illumination BT200100-WHIIC), images of DS-3 have a balanced and homogeneous background. Also, the images are directly saved from the raw video files (.cine) that retain the highest image quality. As such, this pre-processing step was not necessary for DS-3.

The images were categorized into two boiling regimes: (1) The critical heat flux regime (CHF), where a significant drop in the heat transfer coefficient is

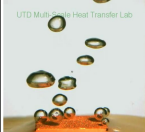



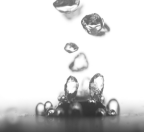
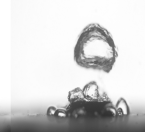
Datasets					
DS-1		DS-2		DS-3	
Pre-CHF	CHF	Pre-CHF	CHF	Pre-CHF	CHF
					
5372 images	786 images	1982 images	1233 images	11724 images	12166 images

Figure 3: Representative images of bubble dynamics from source videos.

observed due to a continuous vapor layer blanketing the heater surface and (2) pre-CHF regime, where optimal heat transfer coefficient is obtained and only discrete bubbles or frequent bubble coalescence is observed before departure. While images of DS-1 and DS-2 have been labeled by the authors of the datasets, this study is designed to be unsupervised learning thus labeling of DS-2 is only used to assess the model performance. Originally, DS-1 had a total of 6158 images (786 CHF versus 5372 pre-CHF), DS-2 had a total of 3215 (1233 CHF versus 1982 pre-CHF) and DS-3 had a total of 23890 (12166 CHF versus 11724 pre-CHF). As seen, all data sets were unbalanced. We used undersampling to balance DS-1. Datasets DS-2 and DS-3 were not balanced since the objective of this study is to introduce a framework that utilizes unsupervised learning, that is, the labeling information of DS-2 and DS-3 are assumed to be unavailable. Table1 shows the number of images in each regime for each dataset before and after the down-sampling process and Fig3 shows a visual representation of the images for each dataset. The pixel intensity values in each image were normalized to fit in the range [0,1] to ensure uniformity over multiple datasets during deep learning training.

DS	Before under-sampling of DS-1		After under-sampling of DS-1	
	CHF	Pre-CHF	CHF	Pre-CHF
DS-1	786	5372	786	786
DS-2	1233	1982	1233	1982
DS-3	12166	11724	12166	11724

Table 1: Datasets Summary

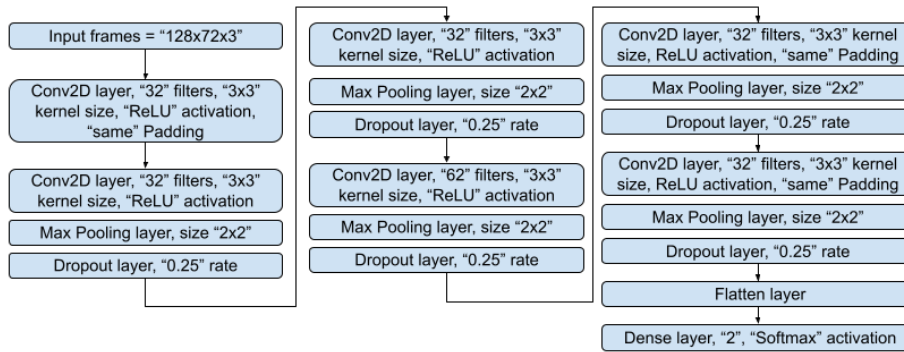


Figure 4: CNN Architecture for the base model.

3.2. Base CNN Model Training

Fig4. illustrates the CNN model architecture adopted in this research. The dataset was divided into three parts: 1) a training set (80%), 2) a validation set (10%), and 3) a test set (10%). The Base CNN model was trained using a batch size = 16 and an Adam optimizer. The training was stopped after 100 epochs and the model that scored the lowest loss on the validation set was selected. Finally, the selected model was blind tested on the test set where the model achieved 99% accuracy.

3.3. Fixed-Point GAN Training

The target dataset was divided into three parts: a) training set, b) validation set, and c) testing set. The training set from the target dataset was fed into the FP-GAN model along with 100% of the source dataset. The GAN model was

trained for 300,000 epochs, where every 10,000 epochs a model was saved. A total of 30 GAN models were saved. To evaluate the model performance, we used the Fréchet Inception Distance (FID) metric. The FID reflects on the difference between two sets of images in terms of statistical vision features. Let $p(\cdot)$ be the distribution of the InceptionV3 model internal representations (activations) of the images generated by the model and $p_w(\cdot)$ the distribution of the same neural network activations from the "world" of real images used to train the model. The FID is basically the difference of the two Gaussians measured by the Fréchet distance also known as the Wasserstein-2 distance. The Fréchet distance $d(\cdot, \cdot)$ between the Gaussian with mean and covariance (m, C) obtained from $p(\cdot)$ and the Gaussian (m_w, C_w) obtained from $p_w(\cdot)$ is called the FID.

$$\begin{aligned} \text{FID} &= d^2((\mathbf{m}, \mathbf{C}), (\mathbf{m}_w, \mathbf{C}_w)) \\ &= |\mathbf{m} - \mathbf{m}_w|_2^2 + \text{Tr}(\mathbf{C} + \mathbf{C}_w - 2(\mathbf{C}\mathbf{C}_w)^{1/2}) \end{aligned}$$

The lower the score, the better the translation quality of the generated images by the GAN. The target validation data was fed into the 30 models to generate synthetic data images that look like source data images. Thus, a total of 30 sets of generated images are to be evaluated. The FID score was used to measure the distance between each of the 30 sets and the real source data images. The model that scored the lowest FID score on the validation set is the model to be selected to translate images from the target domain to the source domain. In theory, the framework process is at an end after selecting the best UI2I translation model to be deployed in production using the FID metric. However, since we do have the labels available, we utilize these labels to see if the framework is in fact doing what it is supposed to be doing in the final testing stage. In this part, we use the CNN model to find the actual best attainable translation FP-GAN model out of the saved 30 and then compare it with the best FID FP-GAN model that was obtained without using the labels. After using the 30 models to generate the 30 newly translated datasets from the same validation set, the Base CNN model was used to classify the newly generated images and the results were evaluated using traditional supervised

Test DS	Balanced Accuracy	F1 weighted	Precision weighted	Recall weighted	ROC AUC
DS-1	0.99	0.99	0.99	0.99	1.00
DS-2	0.50	0.47	0.38	0.62	0.37
DS-3	0.50	0.32	0.24	0.49	0.89

Table 2: Test Results of Base CNN Model on DS-1, DS-2 and DS-3

learning metrics to identify the best attainable FP-GAN model. Afterward, both the best attainable model and the best FID model are used to translate the test data set and then classify both using the Base CNN model and evaluate it to further confirm the results.

4. Experimental Results and Discussion

4.1. Experiment I: Base CNN Model and Blind Cross-Domain Testing

In this section, the results obtained from the Base CNN model training are presented. Moreover, the results will be compared with blindly testing the Base CNN model on the target images directly (without translation). As seen in Table2, while the Base CNN model has satisfactory performance on the source DS which the model was trained and validated on, its performance on the target DS, which is previously unseen by the model is far from being acceptable as expected. This supports our efforts to explore the use of FP-GAN to improve the prediction of unseen data from different sources.

4.2. Experiment II: Base CNN Model on target Images Translated Using FP-GAN

In this experiment, we first apply FP-GAN to render synthetic images from the target DS which is then used as input for the Base CNN model for classification. Once the FP- GAN model started training, the model was saved every 10,000 epochs until the end of the training session that was set to 300,000 epochs. Thus, a total of 30 models were saved. Because of the lack of labels in

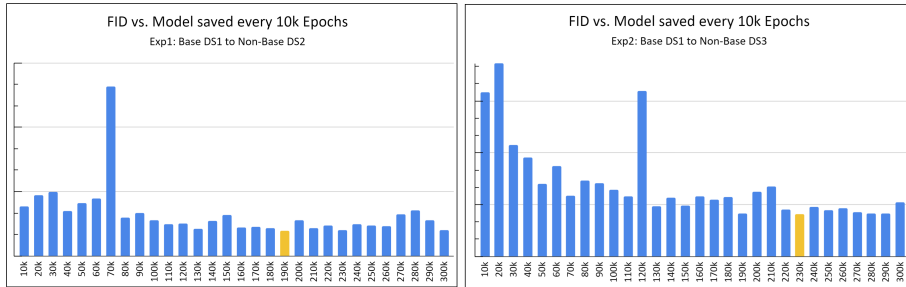


Figure 5: FID Values for Images Generated from the Validation Sets of DS-2 and DS-3 Using the 30 FP-GAN Models.

unsupervised machine learning, traditional supervised evaluation metrics cannot be used in deciding when to stop the model from training. Thus, each of these 30 models was evaluated on the target validation dataset using the unsupervised FID metric. The model that scored the best in the FID metric (lowest value), was selected to be used in rendering generated images from the target test dataset. Fig5 shows the FID values for images generated from the target validation sets of DS-2 and DS-3 using the 30 FP-GAN Models.

As seen in Fig5, the models saved at epochs 190k and 230k were the best FID scoring models for DS-2 and DS-3 respectively. The best FID scoring model was then applied to the target testing data set to translate them into the source DS domain. The target test set images translated by the best FID scoring model were classified using the Base CNN model. The results were then compared with the evaluation results when using the Base CNN model on the same target test set without translation to showcase the efficiency of the proposed framework. The results of this comparison are summarized in Table3. As seen, the model performance is improved on all five evaluation metrics.

4.3. Discussion on FP-GAN for Boiling Crisis Detection

Fig6 shows samples generated from each class for DS-2 and DS-3, respectively. The first row shows samples from the real target DS images, while the second row shows the transformed version of the same image generated using the best FID scoring model.

Metric	DS-2		DS-3	
	w/o translation	with translation	w/o translation	with translation
Balanced Accuracy	0.50	0.75	0.50	0.90
F1 weighted	0.47	0.71	0.32	0.90
Precision weighted	0.38	0.80	0.24	0.90
Recall weighted	0.62	0.71	0.49	0.90
ROC AUC	0.37	0.77	0.89	0.95

Table 3: Base CNN Model Evaluations on DS-2 and DS-3 With and Without Translation

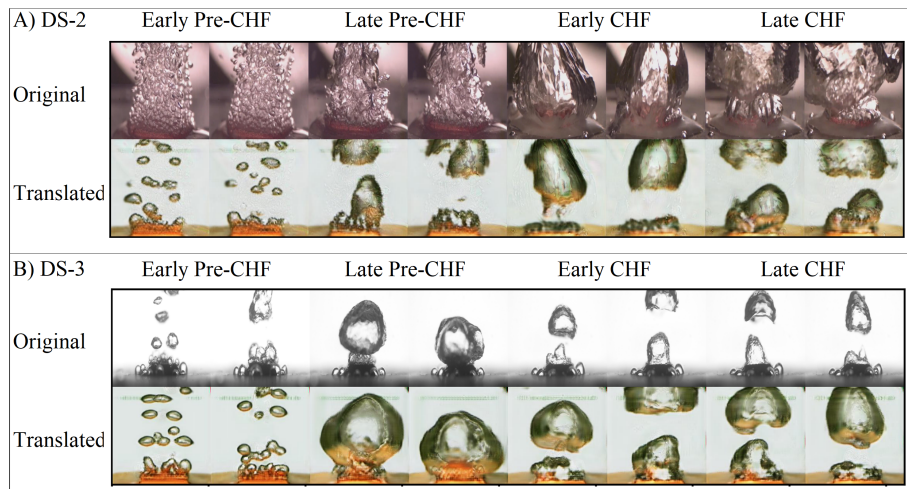


Figure 6: Samples Generated by the best FID Scoring Models for A) DS-2 \rightarrow DS-1 and B) DS-3 \rightarrow DS-1.

The confusion matrices for both datasets are presented in Table 4. As seen, for DS-2, the model was able to predict 118 out of 124 CHF (95.2%) correctly and 111 out of 200 (55.5%) Pre-CHF. For DS-3, the model was able to predict 1109 out of 1216 CHF (91.2%) correctly and 1040 out of 1172 (88.7%) Pre-CHF. We believe this initial effort shows the promise of using our framework to generalize boiling crisis detection models.

For a more in-depth comparative analysis of the results, the confusion matrices of all types of experiments are displayed in Fig 7. The first column (Tables A and D) shows the results of the Base CNN model when tested blindly on

		Source DS-1 to Target DS-2		Source DS-1 to Target DS-3	
		Predicted		Predicted	
		CHF	Pre-CHF	CHF	Pre-CHF
True	CHF	118	6	1109	107
	Pre-CHF	89	111	132	1040

Table 4: Confusion Matrices: Base CNN Predictions on Translated Images from DS-2 and DS-3

(A) Base CNN on Non-Translated DS-2				(B) Base CNN on translated DS-2				(C) Base DS1 on DS-1			
		Predicted				Predicted				Predicted	
		CHF	Pre-CHF			CHF	Pre-CHF			CHF	Pre-CHF
TRUE	CHF	0	124	TRUE	CHF	118	6	TRUE	CHF	80	0
	Pre-CHF	0	200		Pre-CHF	89	111		Pre-CHF	1	79
Balanced Acc. = 50%				Balanced Acc. = 75%				Balanced Acc. = 99%			

(D) Base CNN on Non-Translated DS-3				(E) Base CNN on translated DS-3				(F) Base DS1 on DS-1			
		Predicted				Predicted				Predicted	
		CHF	Pre-CHF			CHF	Pre-CHF			CHF	Pre-CHF
TRUE	CHF	0	1216	TRUE	CHF	1109	107	TRUE	CHF	80	0
	Pre-CHF	0	1172		Pre-CHF	132	1040		Pre-CHF	1	79
Balanced Acc. = 50%				Balanced Acc. = 90%				Balanced Acc. = 99%			

Figure 7: Confusion Matrices of all types of experiments.

target DS images without any translation (worst case scenario). As expected, the results show that the model is not generalizable to foreign datasets and will produce results equivalent to randomly guessing with a balanced accuracy of 50% for both DS-2 and DS-3. The second column (Tables B and E) shows the results when using our framework and how it significantly improves the generalization of the Base CNN model for both DS-2 and DS-3 than when used blindly as in the first column. It also shows how far away is our method from the best-case scenario shown in the third column (Tables D and F) where the Base CNN model was tested on the same dataset that it was previously trained on.

It is observed that there is a significant improvement in the results when the images are first translated from the target DS to look like DS-1 images and then tested by the Base CNN model rather than blindly testing the Base

CNN model on the target DS images without any translation. All metrics have improved significantly, but most importantly, the “balanced accuracy” metric has increased by 50% when using DS-2 as target, and by 80% when using DS-3 as the target. This clearly demonstrates the effectiveness of using FP- GAN in translating the images to a domain that the CNN model has seen before and how this translation will improve the results obtained by the same model on the same images before the translation. To further understand the performance of the model, a comparison between samples from the real and the generated images for each class during different time intervals was plotted for each experiment. Fig8 A), B) and C) shows the comparisons for the “pre-CHF” , while D), E) and F) shows the comparisons for the “CHF” class. As seen when comparing Fig8 A) and B), the model for DS-2 doesn’t seem to be able to identify that the early and intermediate stages “pre-CHF” from DS-2 should be translated to early and intermediate -stages DS-1 “pre-CHF” images, but it has more success in translating the latter stages of DS-2 “pre-CHF” to look like their counterparts in DS-1 “pre-CHF”. This could be one of the reasons behind the misclassifications for this class. Another reason could be attributed to the distortions (or fidelity) of the images. The performance for DS-3 is much better for the “Pre-CHF” class. As seen when comparing Fig8 A) and C), the translated images have much better quality throughout the entire process and with little to no traces of the original domain appearing in most images. The model also seems successful in allocating most images to their proper timeline as in the real images which explain the superiority of the results of DS-3 over DS-2 for this class. The performance of the model in the “CHF” class for DS-2 was much better than the “pre-CHF” class. The model seems to be able to translate each stage of this class to it’s correct counterpart. The translated images such as those viewed in Fig8 E) seem to be exhibiting the same distortion problem as in the case of the “pre-CHF” class. The performance for DS-3 for the “CHF” class is also similar to the DS-2 performance. As seen in Fig8 F); however, the translated images seem to have much better quality throughout the entire process and with little to no traces of the original domain appearing in most images. The model also

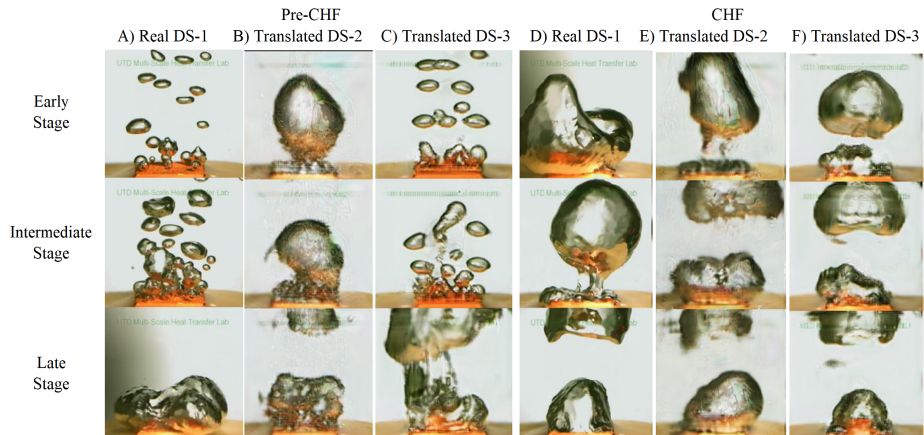


Figure 8: Samples from Real DS-1. Translated DS-2 and Translated DS-3 from Different Stages for Each Regime.

seems successful in allocating most images to their proper timeline as in the real images.

Fig9 A) and B) show a sample of the misclassified images for DS-2 for the “pre-CHF” and the “CHF” classes respectively. As observed, the major reason behind the misclassifications of the “pre-CHF” class for DS-2 is that the translated images look more like the “CHF” class rather than the “pre-CHF” class. The reason for the misclassifications in the “CHF” images for DS-2 could be that the six misclassified images suffer from distortion and immature translation effects. Similarly, Fig9 C) and D) show a sample of the misclassified images for DS-3. All classifications for the “pre-CHF” class are occurring exclusively in the later half of this stage (from 60W to 120W) where the images start to look similar to the “CHF” state as apparent in the figure. Misclassified images from both classes seem to be suffering from apparent immature translation artifacts that we suspect are the major cause for the confusion in the classification.

4.4. Discussion on FID

How good was the FID metric for best model selection? To test this, we assumed the labels for the validation data are available and used balanced accuracy instead of FID for model selection. Fig10 A) and B) show the balanced

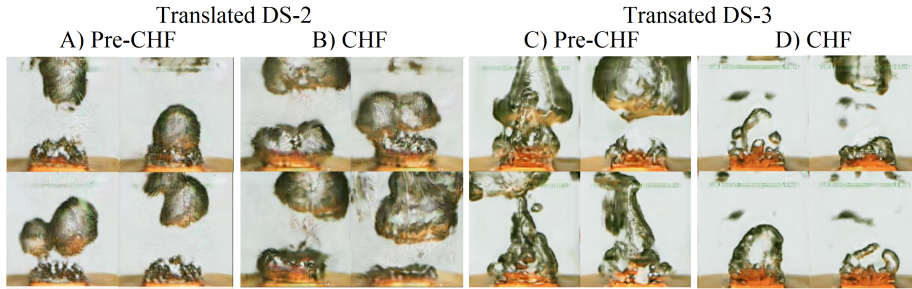


Figure 9: Examples of Misclassified Images from Each DS and Class.

accuracy scores for every model on the labeled validation set for DS-2 and DS-3 respectively. For DS-2, out of the 30 models, the images generated by model 90k achieved the highest balanced accuracy when tested with the Base CNN model with a value of 96% on the validation set compared to 75% achieved by model 190k which was selected by the FID metric. The 90k model was then used to generate fake images from the test set and these images were also tested using the Base CNN model, achieving a balanced accuracy of 95% as compared to the 75% achieved when using the 190k model as seen in Table 5. For DS-3, out of the 30 models, the images generated by model 190k achieved the highest balanced accuracy when tested with the Base CNN model with a value of 98% on the validation set compared to 90% achieved by model 230k that was selected by the FID metric. The 190k model was then used to generate fake images from the test set and these images were also tested using the Base CNN model, achieving a balanced accuracy of 98% as compared to the 90% achieved when using the 230k model as seen in Table 5.

The confusion matrices for both models for DS-2 are displayed in Fig11. There is a notable improvement in the prediction accuracy of the “Pre-CHF” class, it has improved from 56% to 99%, while the predicting accuracy for the “CHF” class slightly decreased from 95% to 91%.

The confusion matrices for both models for DS-3 are displayed in Fig12. There is a notable improvement in the prediction accuracy of both classes. The accuracy for the “pre-CHF” class improved from 89% to 97%, while the

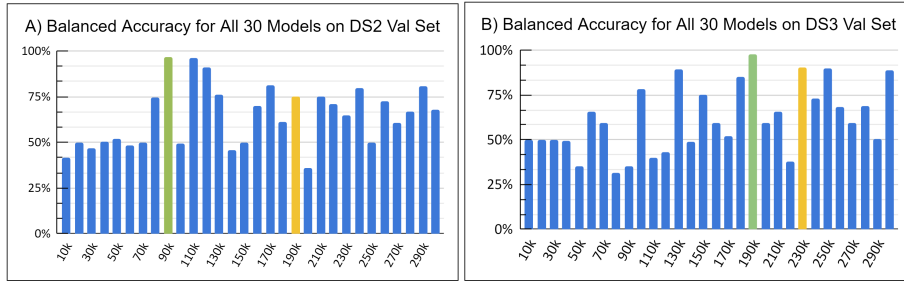


Figure 10: Metrics Comparison Between Best Attainable Models and FID Selected Models on Test Set for DS-2 and DS-3.

DS	Model Name	Balanced Accuracy	F1 weighted	Precision weighted	Recall weighted	ROC AUC
DS-2	90k model	0.95	0.96	0.96	0.96	0.99
	190k model	0.75	0.71	0.80	0.71	0.77
DS-3	190k model	0.98	0.98	0.98	0.98	1.00
	230k model	0.90	0.90	0.90	0.90	0.95

Table 5: Confusion Matrices of Base CNN Predictions on Translated Images from DS-2 and DS-3

		Predicted				Predicted	
		CHF	Pre-CHF			CHF	Pre-CHF
True	CHF	113	11	True	CHF	118	6
	Pre-CHF	2	198		Pre-CHF	89	111

(A) (B)

Figure 11: Confusion Matrices for (A)90k and (B)190k Models.

		Predicted				Predicted	
		CHF	Pre-CHF			CHF	Pre-CHF
True	CHF	1208	8	True	CHF	1109	107
	Pre-CHF	38	1134		Pre-CHF	132	1040

(A) (B)

Figure 12: Confusion Matrices for (A) 190k and (B) 230k Models.

predicting accuracy for the “CHF” class increased from 91% to 99%.

As seen from the results above, in general, although the FID metric provides a good solution, it may not guarantee the best attainable one. We plan to study different GAN metric, for example, distance metric based on the principal component derived from the images (Rokoni et al., 2022) as our immediate next steps.

5. Conclusion

In this paper, we introduced a framework for generalizing boiling crisis detection CNN models using FP-GAN. A CNN model is trained on the base dataset for boiling regime classification (pre-CHF vs. post-CHF). Boiling images from new datasets (no-base datasets) are translated into the base domain using the generator of FP-GAN, and then classified by the base CNN model. Three distinct boiling datasets from different research groups are used to demonstrate the effectiveness of the developed model. The results show that:

1. Domain adaption using FP-GAN yields much higher accuracy than the base CNN model for classifying new datasets without using labels.
2. FID is a generally reliable metric to identify domain adaptation models with good performance. Although it may not always identify the best model, it can pick up a model with reasonably good performance among all the generated models without using labels. Future efforts will be made toward developing more reliable metrics for best model identification.

Compared to existing visualization-based CHF detection studies that are predominately based on datasets with labels, the present work demonstrates the feasibility of classifying boiling images from any new datasets without labels. This work presents a significant step toward developing generalizable deep learning models for engineering applications and making visualization-based boiling crisis a viable monitoring and detection tool in industrial applications. Moreover, The framework could be generalized to work with any classification model (not just CNN) using any UI2I translation model (not just FP-GAN).

CRedit authorship contribution statement

Firas Al-Hindawi: Conceptualization, Methodology, Software, Writing - Original Draft, Writing - Review & Editing. **Tejaswi Soori:** Data Curation, Writing - Original Draft, Writing - Review & Editing. **Han Hu:** Conceptualization, Writing - Original Draft, Writing - Review & Editing, Data Curation. **Md Mahfuzur Rahman Siddiquee:** Conceptualization, Software, Writing - Original Draft, Writing - Review & Editing. **Hyunsoo Yoon:** Conceptualization, Writing - Review & Editing, Supervision. **Teresa Wu:** Conceptualization, Methodology, Writing - Original Draft, Writing - Review & Editing, Resources, Supervision, Project administration. **Ying Sun** Writing - Review & Editing, Supervision.

Declaration of Competing Interest

The authors declare that they have no known competing financial interests or personal relationships that could have appeared to influence the work reported in this paper

Acknowledgement

Support for this work was provided in part by the US National Science Foundation under Grant No. CBET-1705745.

References

- Alhindawi, F., & Altarazi, S. (2018). Predicting the tensile strength of extrusion-blown high density polyethylene film using machine learning algorithms. In *2018 IEEE International Conference on Industrial Engineering and Engineering Management (IEEM)* (pp. 715–719). IEEE.
- Allred, T., Weibel, J., & Garimella, S. (2018). Enabling highly effective boiling from superhydrophobic surfaces. *Phys. Rev. Lett.*, *120*, 174501. doi:10.1103/PhysRevLett.120.174501.

- Altarazi, S., Allaf, R., & Alhindawi, F. (2019). Machine learning models for predicting and classifying the tensile strength of polymeric films fabricated via different production processes. *Materials*, *12*, 1475.
- Bode, M., Gauding, M., Lian, Z., Denker, D., Davidovic, M., Kleinheinz, K., Jitsev, J., & Pitsch, H. (2021). Using physics-informed enhanced super-resolution generative adversarial networks for subfilter modeling in turbulent reactive flows. *Proc. Combust. Inst.*, *38*, 2617–2625,. doi:10.1016/j.proci.2020.06.022.
- Choi, Y., Choi, M., Kim, M., Ha, J., Kim, S., & Choo, J. (2018). Stargan: Unified generative adversarial networks for multi-domain image-to-image translation. In *Proc. IEEE Comput. Soc. Conf. Comput. Vis. Pattern Recognit* (pp. 8789–8797,). doi:10.1109/CVPR.2018.00916.
- Deng, M., Deng, A.-D., Shi, Y., & Xu, M. (2022). Correlation regularized conditional adversarial adaptation for multi-target-domain fault diagnosis. *IEEE Transactions on Industrial Informatics*, .
- Deng, Z., He, C., Liu, Y., & Kim, K. (2019). Super-resolution reconstruction of turbulent velocity fields using a generative adversarial network-based artificial intelligence framework. *Phys. Fluids*, *31*. doi:10.1063/1.5127031.
- Gao, F., Wu, T., Chu, X., Yoon, H., Xu, Y., & Patel, B. (2020). Deep residual inception encoder-decoder network for medical imaging synthesis. *IEEE Journal of Biomedical and Health Informatics*, *24*, 39–49,. doi:10.1109/JBHI.2019.2912659.
- Goodfellow, I., Pouget-Abadie, J., Mirza, M., Xu, B., Warde-Farley, D., Ozair, S., Courville, A., & Bengio, Y. (2014). Generative adversarial nets. *arXiv preprint arXiv:1406.2656*.
- Hassan, M., Huda, S., Sharmeen, S., Abawajy, J., & Fortino, G. (2021-04). An adaptive trust boundary protection for iiot networks using deep-learning feature-extraction-based semisupervised model. *IEEE Transactions on Industrial Informatics*, *17*, 2860–2870,. doi:10.1109/TII.2020.3015026.

- Hobold, G., & Silva, A. (2018). Machine learning classification of boiling regimes with low speed, direct and indirect visualization. *Int. J. Heat Mass Transf.*, *125*, 1296–1309,. doi:10.1016/j.ijheatmasstransfer.2018.04.156.
- Ji, Y., Liu, S., Zhou, M., Zhao, Z., Guo, X., & Qi, L. (2022). A machine learning and genetic algorithm-based method for predicting width deviation of hot-rolled strip in steel production systems. *Information Sciences*, *589*, 360–375.
- Kandlikar, S. (2001). A theoretical model to predict pool boiling chf incorporating effects of contact angle and orientation. *J. Heat Transfer*, *123*, 1071–1079,. doi:10.1115/1.1409265.
- Lee, I., Yoon, D., Bang, Y., Kim, T., & Kim, Y. (2021). Assessment of realistic departure from nucleate boiling ratio (dnbr) considering uncertainty quantification of core flow asymmetry. *Energies*, *14*. doi:10.3390/en14051504.
- Lee, S., & You, D. (2019). Data-driven prediction of unsteady flow over a circular cylinder using deep learning. *J. Fluid Mech.*, *879*, 217–254,. doi:10.1017/jfm.2019.700.
- Li, J., Fu, W., Zhang, B., Zhu, G., & Miljkovic, N. (2019). Ultrascalable three-tier hierarchical nanoengineered surfaces for optimized boiling. *ACS Nano*, *13*, 14080–14093,. doi:10.1021/acsnano.9b06501.
- Minseok, H., Bertina, B., & Graham, S. (2014). Pool boiling experiment.
- Park, Y., Kim, H., Kim, J., & Kim, H. (2016). Measurement of liquid-vapor phase distribution on nano- and microstructured boiling surfaces. *Int. J. Multiph. Flow*, *81*, 67–76,. doi:10.1016/j.ijmultiphaseflow.2016.01.007.
- Rassoulinejad-Mousavi, S., Al-Hindawi, F., Soori, T., Rokoni, A., Yoon, H., Hu, H., Wu, T., & Sun, Y. (2021). Deep learning strategies for critical heat flux detection in pool boiling. *Appl. Therm. Eng.*, *190*, 116940,. doi:10.1016/j.applthermaleng.2021.116849.

- Ravichandran, M., Su, G., Wang, C., Seong, J., Kossolapov, A., Phillips, B., Rahman, M., & Bucci, M. (2021). Decrypting the boiling crisis through data-driven exploration of high-resolution infrared thermometry measurements. *Appl. Phys. Lett*, *118*, 253903,. doi:10.1063/5.0048391.
- Ridwan, S., & McCarthy, M. (2019). Nanostructure-supported evaporation underneath a growing bubble. *ACS Appl. Mater. Interfaces*, *11*, 12441–12451,. doi:10.1021/acsami.8b21260.
- Rokoni, A., Zhang, L., Soori, T., Hu, H., Wu, T., & Sun, Y. (2022). Learning new physical descriptors from reduced-order analysis of bubble dynamics in boiling heat transfer. *International Journal of Heat and Mass Transfer*, *186*, 122501.
- Siddiquee, M., Zhou, Z., Tajbakhsh, N., Feng, R., Gotway, M., Bengio, Y., & Liang, J. (2019). Learning fixed points in generative adversarial networks: From image-to-image translation to disease detection and localization. *Proc. IEEE Int. Conf. Comput. Vis*, (pp. 191–200,). doi:10.1109/ICCV.2019.00028.
- Sinha, K., Kumar, V., Kumar, N., Thakur, A., & Raj, R. (2021). Deep learning the sound of boiling for advance prediction of boiling crisis. *Cell Reports Phys. Sci*, *2*, 100382,. doi:10.1016/j.xcrp.2021.100382.
- Wang, D., Hu, M., & Weir, J. D. (2022). Simultaneous task and energy planning using deep reinforcement learning. *Information Sciences*, .
- Wilson, G., & Cook, D. (2020). A survey of unsupervised deep domain adaptation. *ACM Trans. Intell. Syst. Technol*, *11*. doi:10.1145/3400066.
- Xu, G., Huang, C., Silva, D., & Albuquerque, V. (2022). A compressed unsupervised deep domain adaptation model for efficient cross-domain fault diagnosis. *IEEE Transactions on Industrial Informatics*, . doi:10.1109/TII.2022.3183225.

- You, S. (2014). Pool boiling. URL: <https://msht.utdallas.edu/>.
- Zhao, D., Liu, S., Zhang, T., Zhang, H., & Miao, Z. (2022). Subdomain adaptation capsule network for unsupervised mechanical fault diagnosis. *Information Sciences*, *611*, 301–316.
- Zhu, J.-Y., Park, T., Isola, P., & Efros, A. A. (2017). Unpaired image-to-image translation using cycle-consistent adversarial networks. In *Proceedings of the IEEE international conference on computer vision* (pp. 2223–2232).
- Zuber, N. (1959). Hydrodynamic aspects of boiling heat transfer (thesis. doi:10.2172/4175511).